Chemical Engineering Journal 522 (2025) 168275

Contents lists available at ScienceDirect

Chemical Engineering Journal

journal homepage: www.elsevier.com/locate/cej

A novel BMSCs/GelMA-ACMMA composite hydrogel with tunable viscoelasticity promotes growth plate cartilage repair *via* the Piezo1-ROCK pathway

Guanlu Shen [a,b,1], Xinxin Si [b,1], Lei Qiang [a,1], Yihao Liu [a,1], Zhiyang Yin [a], Jing Shan [c], Pengfei Zheng [a,*]

[a] *Department of Orthopaedic Surgery, Children's Hospital of Nanjing Medical University, Nanjing, 210008, PR China*
[b] *Jiangsu Key Laboratory of Marine Bioresources and Environment, Co-Innovation Center of Jiangsu Marine Bio-industry Technology, Jiangsu Key Laboratory of Marine Pharmaceutical Compound Screening, Jiangsu Ocean University, Lianyungang, 222005, PR China*
[c] *School of Pharmacy, The University of Sydney, Sydney, NSW, 2006, Australia*

ARTICLE INFO

Keywords:
Bone marrow mesenchymal stem cells
Acellular cartilage matrix
Viscoelasticity
Piezo1-ROCK
Growth plate injury repair

ABSTRACT

Growth plate injuries in children and adolescents often lead to bone bridge formation, resulting in limb deformities due to the limited self-repair capacity of the growth plate. The limitations of traditional treatments prompted interest in the role of the extracellular matrix (ECM) and mechanical environment in tissue repair. Recent research showed that 3D hydrogels could mimic ECM to regulate mesenchymal stem cells (MSCs) differentiation, with MSCs sensing matrix viscoelasticity *via* Piezo1 and responding through the ROCK signaling pathway. This study aimed to develop a 3D biomimetic hydrogel composed of acellular cartilage matrix methacryloyl (ACMMA) and gelatin methacryloyl (GelMA), with adjustable viscoelasticity *via* blue light crosslinking time. Hydrogels with low (5 s) and high (20s) modulus were fabricated and loaded with bone marrow mesenchymal stem cells (BMSCs). Results demonstrated that the 5 s hydrogel promoted chondrogenic differentiation and inhibited osteogenesis, effectively preventing bone bridge formation and enhancing growth plate repair *in vivo*. Mechanistic studies confirmed that the 5 s group did not activate the Piezo1-ROCK pathway, supporting its role in chondrogenic differentiation.

1. Introduction

Growth plate (epiphyseal plate) injury is one of the most common skeletal disorders in children and adolescents. The etiology of growth plate injuries is diverse and often associated with fractures, osteomyelitis [1], tumors [2], iatrogenic trauma, or other disease-related factors [3]. The growth plate is a special tissue composed of chondrocytes [4,5]. Its unique three-dimensional structure and biomechanical properties ensure that the growth plate plays an indispensable role in regulating bone development [6]. However, its intrinsic capacity for self-repair is extremely limited [7]. Growth plate injury is typically characterized by the formation of bone bridges [8], which interfere with normal bone elongation and may lead to limb deformities and functional impairments [9].

Current clinical treatments for growth plate injuries primarily include surgical interventions and tissue engineering approaches [10]. Traditional surgical techniques often struggle to fully restore growth plate function. This is due to the complexity of the tissue, low success rates, and a high recurrence rate of bone bridge formation postoperatively [11,12]. Tissue engineering technology mainly includes biological scaffold materials, cells and growth factors [13]. Although there have been certain studies on growth plate cartilage in this field [14], there are still many problems. Conventional scaffold materials often lack key components of natural cartilage. This makes it hard to recreate the necessary biophysical environment for effective regeneration. Consequently, their therapeutic effectiveness *in vivo* is limited [15]. Acellular cartilage matrix (ACM) is an extracellular matrix (ECM)-mimicking scaffold. It retains key bioactive components like collagen and glycosaminoglycans after decellularization [16], providing a chondrogenic microenvironment for cell growth and differentiation

* Corresponding author.
E-mail address: zhengpengfei@njmu.edu.cn (P. Zheng).
[1] Equally contributed to this work: Guanlu Shen, Xinxin Si, Lei Qiang, Yihao Liu

https://doi.org/10.1016/j.cej.2025.168275
Received 14 July 2025; Received in revised form 1 September 2025; Accepted 7 September 2025
Available online 9 September 2025

[17]. However, due to its rapid degradation, ACM can only temporarily delay bone bridge formation [18]. In this study, ACM was modified with methacrylic anhydride (MA) to produce methacrylated ACM (ACMMA), thereby enhancing its mechanical properties. Nonetheless, ACMMA alone exhibits limited structural stability and shape retention, making it unsuitable as a primary carrier for seed cells. To address these limitations, we incorporated gelatin methacryloyl (GelMA), a biocompatible polymer, to create a composite hydrogel with improved properties.

Bone marrow mesenchymal stem cells (BMSCs) have attracted significant attention due to their self-renewal ability and multipotent differentiation potential [19–21]. However, the pathological microenvironment following growth plate injury poses considerable challenges to the survival and differentiation of transplanted BMSCs [22]. Research has demonstrated that encapsulating BMSCs within three-dimensional (3D) hydrogels can better mimic their native morphology and molecular environment, thereby promoting cell viability and function. Moreover, the differentiation fate of BMSCs can be modulated by tuning the mechanical properties of the hydrogel ECM [23,24]. For example, softer hydrogels (~2 kPa) significantly enhance cell viability and upregulate the expression of cartilage-specific matrix proteins. In contrast, stiffer hydrogels (6–60 kPa) typically promote osteogenesis [25]. These findings underscore the critical role of matrix stiffness in directing the osteogenic, adipogenic, and chondrogenic differentiation of BMSCs.

Piezo1, a mechanosensitive ion channel, has been identified as a key regulator in cellular mechanotransduction. It can sense the mechanical properties of the ECM and transduce signals that influence mesenchymal stem cell (MSC) fate [26]. Research demonstrates that higher viscoelasticity in ECM hydrogels activates Piezo1. This triggers elevated intracellular Ca^{2+} in BMSCs, enhancing their osteogenic potential [27,28]. In the context of chondrogenesis, the RhoA-ROCK signaling pathway plays a crucial role in regulating BMSC differentiation. Inhibiting this pathway with the selective inhibitor Y27632 signi [29] ficantly upregulates cartilage-related gene expression and promotes chondrogenic differentiation.

Based on these insights, we propose a composite hydrogel system with tunable mechanical properties. This system serves as an injectable and biomimetic 3D scaffold. It is designed to be loaded with BMSCs (GAMA/BMSCs). This system combines the bioactivity of ACMMA, the mechanical versatility of GelMA, and the regenerative potential of stem cells. By optimizing the hydrogel's mechanical modulus, we aim to regulate the Piezo1-ROCK signaling pathway. This approach promotes BMSC chondrogenesis without relying on external growth factors and supports effective growth plate repair. In this study, we will systematically investigate how hydrogels with different mechanical properties affect BMSC proliferation, differentiation, and growth plate cartilage regeneration. The investigation will include both *in vitro* and *in vivo* experiments. Furthermore, we will define the underlying mechanisms involved. This research will provide a theoretical foundation for optimizing growth plate tissue engineering strategies. It will also offer scientific and technical guidance for clinically treating growth plate injuries, contributing to the progress of cartilage regenerative medicine.

2. Materials and methods

2.1. Preparation of ACM

Pig ears were purchased from a local market near the laboratory. The cartilage was carefully separated from the surface skin using a surgical scalpel, retaining only the pure auricular cartilage tissue. The cartilage was then rinsed with deionized water and cut into small pieces. After freeze-drying, the cartilage tissues were ground into a fine powder using an automated cryogenic sample grinder (provided by Shanghai Jingxin Industrial Development Co., Ltd., China). An appropriate amount of cartilage powder was added to phosphate-buffered saline (PBS) containing 0.5 wt% trypsin and 0.02 wt% EDTA and incubated at 37 °C with constant shaking for 24 h. During this process, the trypsin solution was replaced with a fresh one every 4 h. After centrifugation and removal of the supernatant, the pellet was sequentially treated with 10 mM Tris-HCl buffer (pH 7.5) containing 50 U/mL DNase and 1 U/mL RNase A for 4 h, followed by treatment with 10 mM Tris-HCl buffer containing 10 KIU/mL aprotinin for 20 h. Subsequently, the samples were treated with 1 % Triton X-100/PBS solution for 24 h. The material was then washed with deionized water 4–6 times and freeze-dried. The resulting decellularized cartilage powder (10 mg/mL) was enzymatically digested in PBS containing 2 mg/mL pepsin (pH adjusted to 2–3 using glacial acetic acid) at 37 °C with constant shaking for 24 h. After centrifugation, the viscous supernatant was collected, and the pH was neutralized to 7 by adding an appropriate amount of 5 M NaOH. The solution was dialyzed against deionized water using a 3500 Da molecular weight cut-off dialysis membrane for 72 h. Finally, the obtained ACM solution was freeze-dried and stored at −20 °C for further use. All reagents used in the experiments were purchased from Sigma-Aldrich.

To evaluate the decellularization efficiency, the extracellular matrix (ECM) components—glycosaminoglycans (GAGs), collagen, and DNA of native cartilage and decellularized cartilage matrix (ACM) were quantitatively analyzed. Specifically, both native cartilage and ACM samples were digested in a papain solution (125 μg/mL papain, 0.1 M Na_3PO_4, 5 mM Na_2EDTA, 5 mM L-cysteine hydrochloride, pH 6.5) at 60 °C for 12 h. The digestion mixtures were centrifuged at 10,000 *g* for 30 min, and the supernatants were collected. Quantification was then performed following the protocols of the GAG Quantification Assay Kit (Genmed, China), Hydroxyproline Assay Kit (Solarbio, China), and High-Sensitivity Double-Stranded DNA Quantification Kit (Yeason, China). In addition, histological evaluation of decellularization efficiency was conducted using H&E and DAPI staining on tissue sections.

2.2. Preparation and characterization of ACMMA

Following previously reported synthesis methods [30,40], we prepared a photocrosslinking ACMMA hydrogel by reacting decellularized cartilage matrix (ACM) with methacrylic anhydride (MA). Briefly, 1 g of ACM was dissolved in 10 mL of PBS. The pH was adjusted to 8.5–11 using 5 M NaOH, and the solution was transferred to a three-neck flask. After sealing with a rubber stopper and purging with nitrogen (N_2), 1.5 mL of MA was added. The reaction was carried out in a 37 °C water bath under stirring for 3–5 h. The reaction was then terminated by adding PBS (pH 8.5). The resulting solution was dialyzed using a 3500 Da dialysis membrane for 5 days and then lyophilized for further use. To verify the successful grafting of MA onto ACM, both lyophilized ACM and ACMMA were dissolved in deuterium oxide (D_2O) and analyzed using proton nuclear magnetic resonance (^1H NMR), with chemical shifts recorded in parts per million (ppm). Fourier-transform infrared spectroscopy (FTIR) was also used to characterize the chemical composition of ACM and ACMMA within the wavenumber range of 4000–500 cm^{-1}. Additionally, X-ray photoelectron spectroscopy (XPS) was utilized to evaluate the chemical modification status of the materials. To evaluate gelation properties, 10 wt% ACMMA solution was poured into a transparent round-bottom glass vial placed at an angle and exposed to blue light for 30 s to assess hydrogel formation. Additionally, a small amount of red ink was mixed into the ACMMA solution, and the mixture was loaded into a 1 mL syringe (needle diameter 0.5 mm) to draw patterns on a flat surface, thereby testing the injectability and pattern stability of the hydrogel.

2.3. Preparation and characterization of composite hydrogels

2.3.1. Preparation of composite hydrogels

ACMMA solution containing 0.5 wt% photoinitiator was mixed with GelMA solution at various ratios. The mixtures were stirred at 37 °C under light-protected conditions until homogeneous, resulting in 11 groups of composite hydrogels with different compositions. These

hydrogels were then characterized and screened to select one optimal formulation. To obtain composite hydrogels with different moduli, the selected formulation was exposed to blue light for varying crosslinking times (5 s, 10s, 20s, and 30s). After exposure to blue light for 30 s, the composite hydrogel solutions were solidified and demoulded for further use. The compositions and abbreviations of the different hydrogel formulations are listed in Table S1.

2.3.2. Mechanical characterization

Cylindrical composite hydrogel samples were subjected to compression testing using a mechanical testing machine (Hengyi, China) at a constant strain rate of 1 mm/min and a temperature of 25 °C. The test frequency ranged from 0.1 to 5 Hz. The elastic modulus was calculated from the slope of the stress-strain curve within the 0 %–20 % strain range. Rheological measurements were conducted using a Haake Mars modular advanced rheometer (Thermo Fisher Scientific, USA). Steady shear viscosity tests were performed at room temperature under a constant shear rate (0.1–100 s^{-1}) to evaluate the viscosity characteristics of various hydrogels. Frequency sweep tests were conducted under a fixed strain of 1 %, with a frequency range of 0.1–100 rad/s, to determine the storage modulus (G′) and loss modulus (G″).

2.3.3. Physicochemical characterization

To observe the internal morphology and structure of the composite hydrogels, the samples were freeze-dried, fractured in liquid nitrogen, gold-sputtered, and imaged using a scanning electron microscope (SEM; TESCAN, Czech Republic). Meanwhile, X-ray diffraction (XRD; Empyrean, PANalytica) was used to further characterize the internal structure of the composite hydrogel using Co-Kα radiation with a scanning range of 10° to 90°. For swelling performance evaluation, freeze-dried hydrogels were first weighed (Md), and then immersed in PBS at room temperature for 24 h. After full swelling, excess surface water was removed using filter paper, and the swollen weight (Mw) was recorded. The swelling ratio was calculated using the formula:

$$\text{Swelling ratio} = \frac{M_w}{M_d}$$

For degradation analysis, freeze-dried composite hydrogels were initially weighed (M_0), then immersed in PBS at 10 mg/mL concentration and incubated at 37 °C. Samples were retrieved and freeze-dried at 5 different time points (days 3, 7, 14, 21, and 28), and the dry weight was recorded as Mt. The degradation ratio was calculated using the formula:

$$\text{Degradation} = \frac{M_0 - M_t}{M_0} \times 100\%$$

2.4. Preparation of BMSCs-loaded composite hydrogels

2.4.1. Isolation and culture of BMSCs

Bone marrow-derived mesenchymal stem cells (BMSCs) were isolated from the femoral and tibial bone marrow cavities of 3–4-week-old male Sprague-Dawley (SD) rats [31]. The harvested cells were cultured in α-MEM medium supplemented with 10 % fetal bovine serum and 1 % penicillin-streptomycin at 37 °C in a humidified atmosphere containing 5 % CO_2. The culture medium was replaced every 3 days. When the cells reached 90 % confluency, they were passaged. Cells from passages 3 to 5 were used in subsequent experiments to ensure viability and differentiation potential.

2.4.2. Cell encapsulation in hydrogels

The composite hydrogel precursor solution containing 0.5 wt% photoinitiator was premixed with BMSCs at a final cell density of 1×10^7 cells/mL [32]. The cell-laden precursor solution was dispensed into well plates and photo-crosslinked under different exposure times. After gelation, chondrogenic induction medium was added, which contained 1 mM sodium pyruvate (G4212, Cevier), 40 ng/mL dexamethasone (D137736, Aladdin), 50 μg/mL L-ascorbic acid (A800295, Macklin), 46 μg/mL L-proline (L816039, Macklin), and 1 % ITS-G (G4028, Cevier). The hydrogels were cultured at 37 °C in a 5 % CO_2 incubator for 14 days, with the medium changed every 3 days.

2.5. In vitro studies

2.5.1. Biocompatibility

In vitro biocompatibility experiments included cell viability and proliferation assays. To assess cell viability, the composite hydrogel precursor solution containing 1×10^7 cells/mL of BMSCs was cultured in confocal dishes for 5 days. A staining solution was prepared at a ratio of 2 mL PBS: 1 μL AM: 1 μL PI (Calcein-AM/PI), and the staining solution was added to each group. The samples were incubated at 37 °C in the dark for 20 min, followed by imaging of live/dead cells using a confocal laser scanning microscope and quantitative analysis was performed using ImageJ. Additionally, the composite hydrogel precursor solution containing 1×10^7 cells/mL of BMSCs was cultured in 12-well plates for 1, 3, and 5 days. Then, 100 μL of CCK-8 solution (Selleckchem) was added to each well, and the plates were incubated at 37 °C in the dark for 4 h. The absorbance was measured at 450 nm using a microplate reader (Bio-Tek) after transferring 100 μL of the supernatant into a 96-well plate.

2.5.2. Cartilage matrix formation assay

The formation of the cartilage matrix was assessed by Alcian blue staining of the frozen sections of composite hydrogels loaded with BMSCs. Images were captured using an inverted microscope to evaluate the formation of proteoglycans in the cartilage matrix. Quantitative analysis of the Alcian Blue staining results was conducted using ImageJ software (with a quantitative area of 6 cm^2), to verify the effect of promoting BMSC cartilage differentiation in different modulus composite hydrogels.

2.5.3. Gene expression

To release the encapsulated cells, type II collagenase (BioFroxx) was used to digest the hydrogel at 37 °C for 1 h. Total RNA was extracted from the cells using the MolPure® Cell/Tissue Total RNA Kit, followed by reverse transcription to cDNA using the Hifair® II 1st Strand cDNA Synthesis SuperMix. RT-qPCR was performed using Hieff® qPCR SYBR Green Premix. Relative gene expression was quantified using the $2^{-\Delta\Delta Ct}$ method. Three independent experiments were conducted, and the primer sequences used are shown in Table S2.

2.5.4. Western blot analysis

After digesting the hydrogel with type II collagenase (BioFroxx) at 37 °C for 1 h, total protein was extracted using the Column Animal Tissue/Cell Total Protein Extraction Kit (PC201, Epizyme Bio). The samples were centrifuged at 15,000 rpm for 30 s at 4 °C to collect the supernatant. Protein concentration was quantified using the BCA Protein Assay Kit (Biotime) and mixed with loading buffer (Epizyme Bio). Equal amounts of protein (40 μg) were loaded onto sodium dodecyl sulfate-polyacrylamide gel electrophoresis (SDS-PAGE). After protein separation, the proteins were transferred onto a polyvinylidene fluoride (PVDF, Thermo Fisher) membrane. The PVDF membrane was blocked with 5 % bovine serum albumin for 1 h and then incubated overnight at 4 °C with the corresponding primary antibody. After washing with 1× TBST, the membrane was incubated with a secondary antibody at room temperature for 1 h. The results were visualized using the Enhanced Chemiluminescence (ECL) kit (Biomart, China) and quantified using Image J software. The primary antibodies used in this experiment are listed in Table S3.

2.5.5. Immunofluorescence analysis

All samples were fixed with 4 % paraformaldehyde for 30 min,

followed by two washes with PBS. The samples were then permeabilized with 0.3 wt% Triton X-100 for 15 min and blocked with 5 % bovine serum albumin at room temperature for 1 h. Afterward, the samples were incubated overnight at 4 °C with primary antibodies (*COL I*, *COL II*, and *COL X*). After washing with PBS three times, the samples were incubated with fluorescent secondary antibody at room temperature for 1 h and stained with DAPI for 6–8 min to visualize the cell nuclei. Finally, the cells were observed under a laser scanning confocal microscope (Leica). The primary antibodies used in the immunofluorescence are listed in Table S3.

2.6. In vivo study

2.6.1. Animal growth plate defect model

All procedures were in accordance with the guidelines for the care and use of laboratory animals set by the National Institutes of Health and approved by the Ethics Committee of Nanjing Medical University. As mentioned, 24 male New Zealand white rabbits, aged 6 weeks, were purchased as the study subjects and randomly divided into three groups (n = 6/group): control group (NC), low modulus scaffold group (5 s), and high modulus scaffold group (20s). After successful anesthesia, the surgical area of the lower limb of the rabbits was prepared, disinfected with iodine cotton balls, and deionized with 75 % ethanol. A longitudinal incision of approximately 2 cm was made on the medial side of the knee joint to the proximal medial tibia. The exposed growth plate was selected as the drilling site, and an oral polishing drill was used at a speed of 10,000 rpm to vertically drill into the tibia, creating a horizontal defect (6 mm long, 2 mm wide, 3 mm deep) [33]. According to the group allocation plan, the hydrogel pre-polymer solution of each group was dripped into the defect area using a syringe and filled. Each group was then treated with *in situ* blue light irradiation to cure for 5 s and 20s, respectively. The subcutaneous tissue was sutured layer by layer, and the skin was intermittently sutured. The rabbits were raised normally postoperatively without the need for fixation. Penicillin was injected daily within 3 days post-surgery to prevent infection. One month and three months after the surgery, the rabbits were euthanized, and the proximal tibial specimens were collected for macroscopic photography and micro-CT scanning. The specimens were then subjected to histological sectioning and stained with H&E, Masson's trichrome, and toluidine blue (TB) to evaluate the regeneration and repair of the growth plate cartilage in each group.

2.6.2. Micro-computed tomography (Micro-CT)

After 3 months, the New Zealand white rabbits were euthanized using carbon dioxide asphyxiation, and the tibiae were collected. Following the previously described method, the morphological parameters of the tibial samples were analyzed using micro-computed tomography (Micro-CT, ZKKS-MCT-Sharp-III scanner, Caskaishen, China) [34]. Three-dimensional reconstruction and image capture of the growth plates were performed using Mimics Research 19.0 software. Then, the bone volume fraction (BV/TV), bone density (Tb.BMD) were analyzed.

2.6.3. Histological staining analysis

The New Zealand white rabbits were euthanized by intravenous air injection, and both tibiae were collected. The tibial samples were fixed in 4 % paraformaldehyde for 48 h and then subjected to a 4-week decalcification process. After decalcification, the samples were embedded in paraffin and sectioned into 4 μm thick sagittal slices. The sections were then deparaffinized and hydrated, followed by sequential staining with H&E, Masson, and TB (toluidine blue) stains. The repair effect of the growth plate was analyzed using the ImageJ software.

2.7. Statistical analysis

All experiments were repeated at least three times, and the results are presented as "mean ± standard deviation." Statistical analysis was performed using SPSS 23.0. Statistical graphs were created using GraphPad Prism 9.5 and Origin. One-way analysis of variance (ANOVA) and *t*-tests were used to compare data within groups. A significance level of $p < 0.05$ was considered statistically significant.

3. Results and discussion

3.1. Preparation and characterization of ACM and ACMMA

To obtain an ECM-biomimetic ACM, pig ear cartilage was selected as the raw material. An effective decellularization method was applied to successfully extract ACM by skin removal, chopping, enzymatic digestion, and freeze-drying treatment (Fig. 1A). Initially, glycosaminoglycans (GAGs) and collagen in ACM were quantitatively analyzed. The results showed that the GAG content in ACM was 254.53 ± 7.02 μg/mL, and the collagen content was 37.04 ± 0.067 μg/mL. Approximately 77.43 % of the GAG components (Fig. 1B) and 53.36 % of the collagen (Fig. 1C) were retained after decellularization. The DNA content was only 38.93 ng/mg, indicating about 96.82 % of the DNA was removed (Fig. 1D). Additionally, H&E staining (Fig. 1E) and DAPI staining (Fig. 1F) of native and decellularized cartilage sheets showed that nearly all nuclei were removed in the decellularized tissues, indicating effective decellularization. Compared to the native group (*i.e.*, untreated samples with 100 % retention), the results showed effective retention of most ECM components alongside near-complete DNA removal. This confirms ACM as a model ECM scaffold supporting chondrocyte growth and avoiding immune rejection reactions [35].

Although ACM contains key components similar to those of natural tissue and mimics the native microenvironment, it still has limitations. Its poor constructability and unstable mechanical properties hinder its practical application [36,37]. Therefore, we modified ACM with methacrylic anhydride (MA) to synthesize a photo-crosslinking methacrylate-modified decellularized cartilage matrix hydrogel (ACMMA). The chemical groups in the hydrogel changed after crosslinking, as indicated by the ^{1}H NMR and FTIR spectra. As shown in Fig. 1G, the ^{1}H NMR spectrum of ACMMA showed signals for methacrylamide groups at 5.4 and 5.6 ppm [38,39]. Additionally, the FTIR spectrum in Fig. 1H showed characteristic peaks of conjugated amide groups. These included the C═O stretching vibration at 1654 cm^{-1} (amide I band), N—H vibration peaks at 3318 cm^{-1} and 3075 cm^{-1} (amide II band), and a C—N absorption peak at 1542 cm^{-1} (amide III band) [40]. These characteristic peaks collectively confirm the successful formation of amide bonds and the C—O stretching vibration from the anhydride at 1029 cm^{-1} also exhibited a significant absorption peak [41]. Furthermore, through a systematic comparison of XPS spectra of ACM and its modified derivative ACMMA, the successful methacrylation reaction was clearly confirmed. As shown in Fig. S1A,B, both ACM and ACMMA exhibit survey spectra featuring only C, O, and N elements, with no detectable impurities, indicating that the methacrylation process did not introduce extraneous heteroatoms. In the high-resolution spectra (Fig. S1C,D), the C 1 s region of ACMMA shows a pronounced increase in the O–C=O feature at 288.56 eV, corresponding to ester carbon atoms derived directly from the newly introduced methacryloyl groups (–COO–) [42]. Simultaneously, the enhancement of the C–O/C–N peak at 286.05 eV further supports the formation of carbon-oxygen single bonds characteristic of ether or ester linkages [43]. Additionally, the O 1 s spectrum exhibits an increased proportion of the O—C component at 532.91 eV, consistent with the augmented ester bond content due to methacrylic ester incorporation [44]. Notably, the N 1 s spectrum, with peaks at 399.35 eV and 401.02 eV, remains unchanged before and after modification. This indicates that the amide nitrogen environment is preserved, and that the modification occurred selectively at hydroxyl sites. Collectively, these results demonstrate that methacryloyl groups were efficiently and selectively grafted onto the ACM molecular backbone, successfully yielding the target product ACMMA. Moreover, the ACMMA

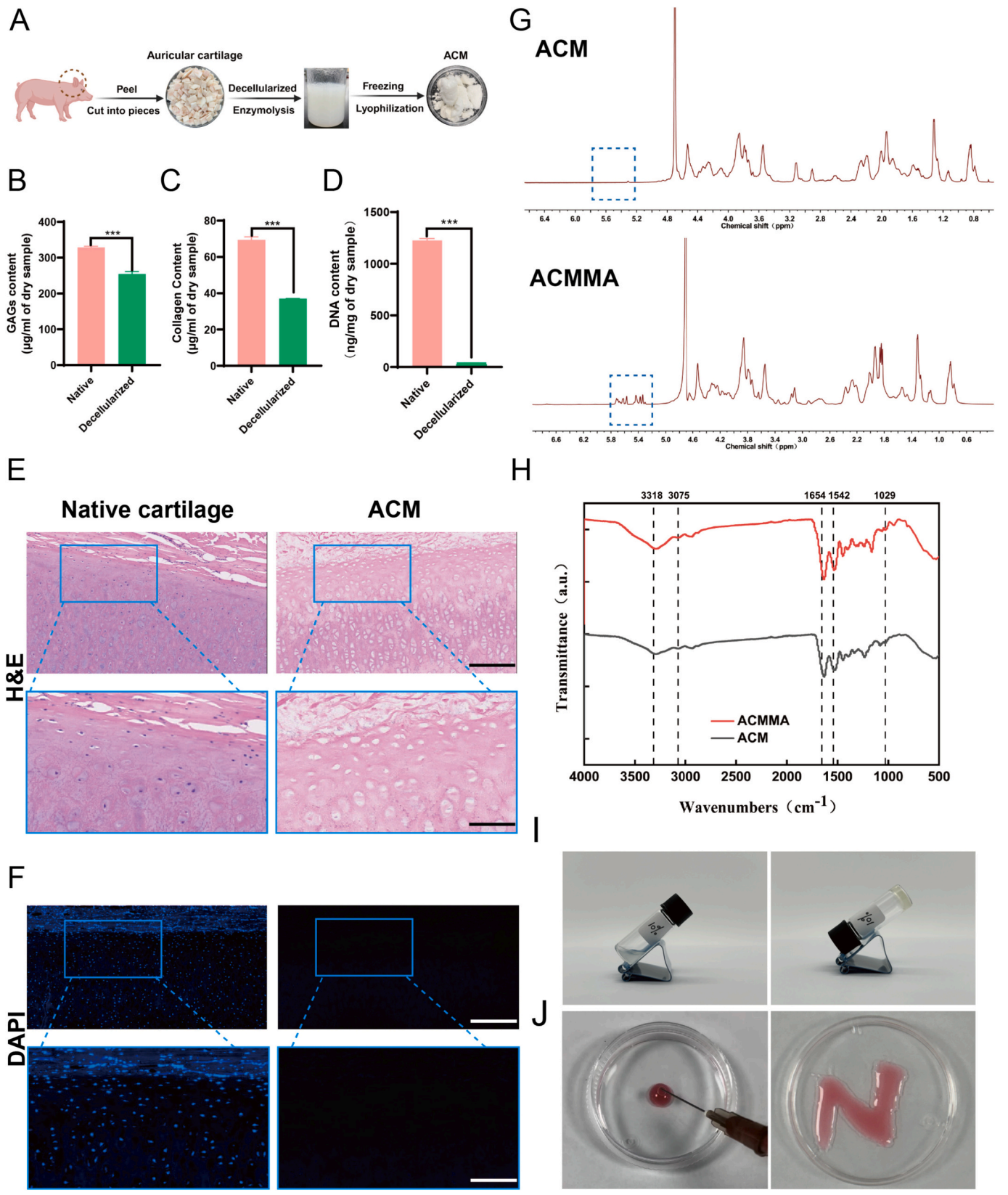

Fig. 1. Preparation and characterization of ACM and ACMMA hydrogels. A) Schematic of the decellularization and enzymatic digestion process used to prepare decellularized pig ear cartilage (Created using BioRender.com). B), C), and D) Quantification of glycosaminoglycan (GAG) content, collagen content, and DNA content before and after decellularization ($n = 3$). E) and F) H&E and DAPI staining images of pig ear cartilage before and after decellularization (original image scale bar: 200 μm; magnified image scale bar: 80 μm). G) ^{1}H NMR spectra of ACM and ACMMA. H) FTIR spectra of ACM and ACMMA. I) Gelation image of ACMMA hydrogel after blue light exposure. *J*) Injection performance characterization of ACMMA hydrogel.

hydrogel can form a stable three-dimensional crosslinked network. The gelation and injectability of the ACMMA hydrogel are shown in Figs. 1I-J. The prepolymer solution of ACMMA, before blue light crosslinking, is a flowing liquid. However, after 30 s of blue light crosslinking, the ACMMA prepolymer solution solidified into a gel and could be smoothly extruded from the syringe to form the desired shape.

3.2. Preparation and characterization of GelMA/ACMMA composite hydrogels with different ratios

Although ACMMA hydrogels exhibit favorable injectability and photo-crosslinking behavior, their structural integrity and shape retention are limited. This restricts their use as the primary material for cartilage tissue engineering. Therefore, we incorporated GelMA to optimize its properties and supplement the collagen components lost during the decellularization process, thereby improving the overall performance of the material. Fig. S2 shows the stress-strain curves and elastic modulus analysis (0–20 % strain slope) of composite hydrogels with different ratios. The results indicate that higher ACMMA content reduces the mechanical strength of the hydrogels. Previous studies have demonstrated that a microenvironment with an elastic modulus in the range of 5–15 kPa closely mimics the mechanical properties of the native cartilage matrix. Such conditions are favorable for directing stem cell differentiation toward the chondrogenic lineage [6,45]. Therefore, four composite hydrogel groups (G7A3, G6A4, G5A5, and G4A6) were selected as the optimal modulus range for chondrocyte differentiation and further characterized. The four hydrogel groups were then freeze-dried in liquid nitrogen and cryogenically fractured. Scanning electron microscopy (SEM) was used to observe the cross-sectional morphology of the hydrogel scaffolds (Fig. 2A). The SEM images revealed that the cross-sections of all hydrogel scaffolds exhibited a sponge-like, porous structure, providing good internal support and stability for the hydrogels. This structure also facilitated the transport of nutrients and the removal of metabolic waste, creating an ideal microenvironment for cell adhesion, growth, and migration [46].

Rheological results (Fig. 2B) indicated that when the angular frequency varied from 0.1 to 100 rad·s^{-1}, the storage modulus (G') of all hydrogel groups was significantly higher than the loss modulus (G"), demonstrating a stable gel state within the hydrogels. Moreover, the results from the flow viscosity tests (0.1–100 s^{-1}) showed that as the proportion of ACMMA in the pre-polymer solution increased, the viscosity of the solution decreased at room temperature (Fig. 2C). Swelling and degradation properties are also critical for hydrogel performance. The G7A3 group showed a swelling ratio similar to the other groups. It had a high water absorption capacity and maintained mechanical stability. This creates an ideal environment for cell adhesion, growth, and metabolism (Fig. 2D) [40]. Regarding degradation performance, the G7A3 group exhibited a degradation rate of 57 % ± 2 %, which was significantly lower than the other groups, showing more persistent stability (Fig. 2E). This relatively slow degradation rate provides longer-lasting structural support, which is essential for cartilage tissues that require continuous repair. It also benefits the long-term adhesion and differentiation of stem cells [47]. Therefore, based on the comprehensive screening results, the G7A3 group is more suitable for cartilage tissue engineering and growth plate repair.

3.3. Preparation and characterization of hydrogels with different moduli

Previous studies have demonstrated that matrix mechanical properties play a critical role in stem cell differentiation. Substrates with different stiffnesses can induce stem cells to differentiate into specific tissue types [47–49]. Therefore, we optimized the light-crosslinking time and conducted stress-strain testing to obtain two sets of composite hydrogels with different moduli, specifically the 5 s and 20s groups. The elastic moduli of these two hydrogels were 5.62 ± 0.94 kPa and 10.21 ± 1.34 kPa, respectively (Fig. 2F and G). As shown in Fig. 2H, rheological results indicated that the G' and G" curves of both groups did not overlap. The storage modulus (G') was much higher than the loss modulus (G"), confirming successful crosslinking in both hydrogels and the 5 s group had a lower G' compared to the 20s group. SEM images (Fig. 2I) showed that both the 5 s and 20s composite hydrogels formed distinct porous structures and the pores in the 20s group were larger than that in the 5 s group. This difference is linked to the higher cross-linking density from the longer cross-linking time [50]. Subsequently, the XRD patterns revealed the internal structural characteristics of ACMMA, GelMA, and the composite hydrogels with different cross-linking times (5 s and 20 s). As shown in Fig. S3, all samples are predominantly amorphous, while significant differences exist in their local ordered structures. GelMA exhibited distinct diffraction peaks at 13.5° and 19.9°, reflecting the presence of certain ordered structures. ACMMA showed characteristic peaks at 14.1° and 18.8°, suggesting a locally ordered structure as well. Compared with the single-component hydrogels, the 5 s composite hydrogels exhibited only weak and broad diffraction peaks at 13.6° and 19.9°, which are indicative of a loose amorphous network. In contrast, the 20s composite hydrogels showed a relatively strong peak at 13.8° and 20.6°, suggesting a more compact internal structure. Therefore, the results demonstrate that crosslinking time significantly affects the internal structure of the composite hydrogels: short crosslinking time (5 s) leads to a softer and highly hydrated network, while long crosslinking time (20s) results in a denser structure with higher rigidity [51,52]. Finally, we evaluated the swelling and degradation properties of the two sets of composite hydrogels. The results showed that the swelling rate of the hydrogels decreased with increasing crosslinking degree (Fig. 2J). All hydrogels remained stable in PBS for over 28 days (Fig. 2K), meeting the requirements for BMSC differentiation and growth plate repair.

3.4. In vitro biocompatibility of scaffold materials

The growth plate is primarily composed of hyaline cartilage, and the biocompatibility of the filling material directly affects the repair outcomes of growth plate injuries [53]. Firstly, live/dead cell staining (Fig. 3A-B) showed very few dead cells (red) in the lower modulus 5 s group. In contrast, a small number of dead cells were observed in the higher modulus 20s group, and the percentage of dead cells was 1.6 %. However, both groups exhibited a large number of live cells (green), indicating that the hydrogels with both moduli have good biocompatibility and can provide a suitable environment for the survival of BMSCs. The results of the CCK-8 assay (Fig. 3C) further confirmed that as the culture time increased, BMSCs in both the 5 s and 20s hydrogels showed proliferative activity. This indicates that both hydrogel moduli promote cell proliferation effectively.

3.5. Chondrogenic differentiation ability of BMSCs on different scaffold materials in vitro

The *in vitro* chondrogenic induction properties of materials are crucial for cartilage differentiation and regeneration. To evaluate the effect of different modulus 3D composite hydrogel scaffold materials on the chondrogenic differentiation of BMSCs, BMSCs were encapsulated in the hydrogels. Then, photo-crosslinked was performed for either 5 s or 20s. The scaffolds were then cultured with a chondrogenic induction medium for 3 weeks. As shown in Fig. 4A, Alcian Blue staining revealed blue cartilage-like lacunae in both the 5 s and 20s hydrogel groups [54]. The quantitative analysis of cartilage cell generation numbers in each group (Fig. S4) further indicated that both hydrogel groups promoted BMSCs chondrogenic differentiation macroscopically. The RT-qPCR results (Fig. 4B-D) showed that, compared to the 2D control group (NC), the expression levels of *Col II* and *Sox9* were significantly upregulated in the 3D hydrogels at both 5 s and 20s. This indicates that the 3D hydrogels more effectively promote the differentiation of BMSCs into chondrocytes [55]. Regarding osteogenic differentiation-related genes,

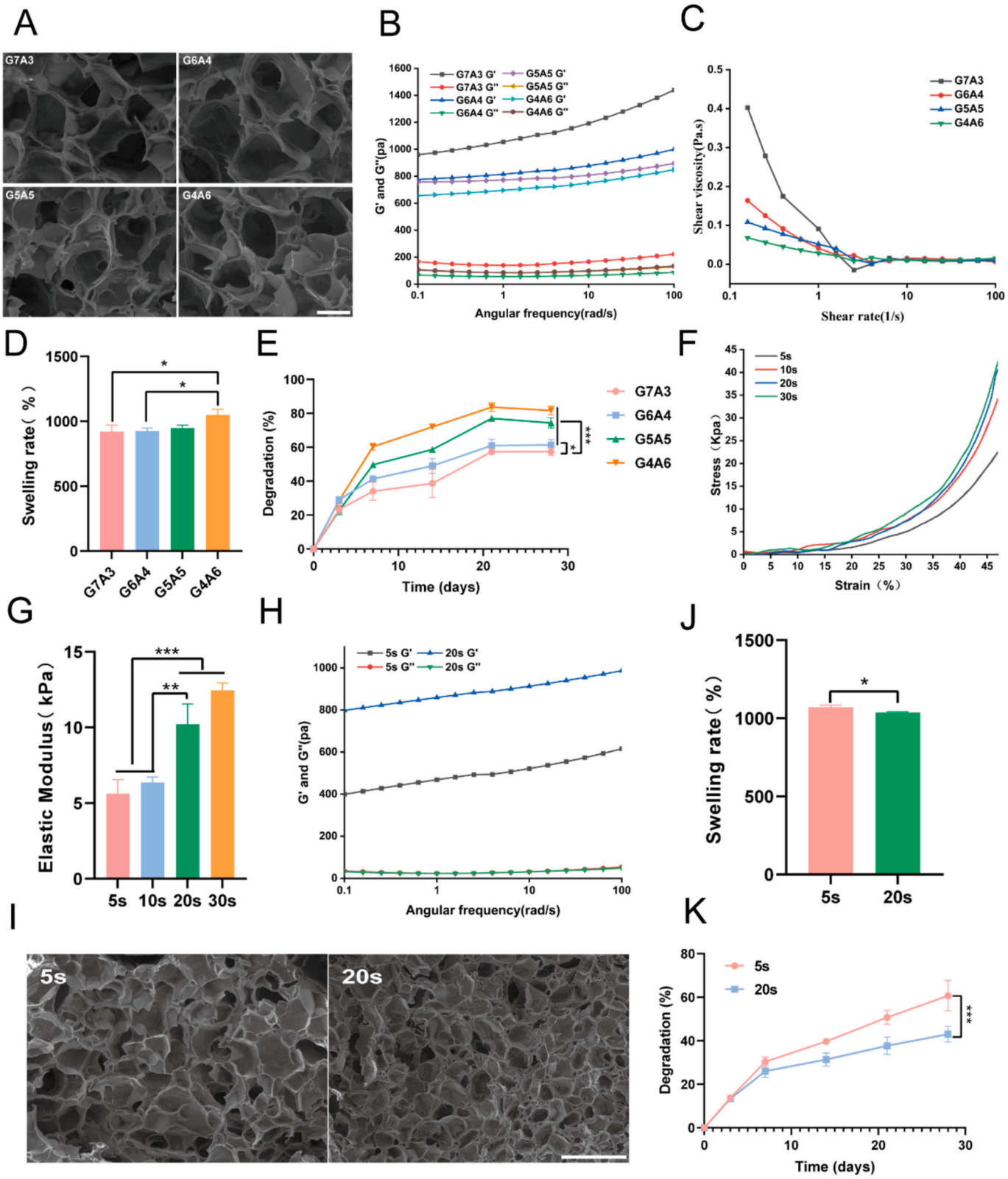

Fig. 2. Preparation and Characterization of Composite Hydrogels. A) SEM images of hydrogels with different ratios of GelMA and ACMMA (scale bar: 50 μm). B) and C) Rheological analysis of hydrogels with different ratios. D) and E) Swelling and *in vitro* degradation characteristics of hydrogels with different ratios ($n = 3$). F) and G) Stress-strain curves and elastic modulus quantification of hydrogels with different moduli ($n = 3$). H) Storage modulus and loss modulus of hydrogels with different moduli. I) SEM images of hydrogels with different moduli (scale bar: 200 μm). J) and K) Swelling and *in vitro* degradation evaluations of hydrogels with different moduli ($n = 3$). (*$p < 0.05$, **$p < 0.01$, ***$p < 0.001$).

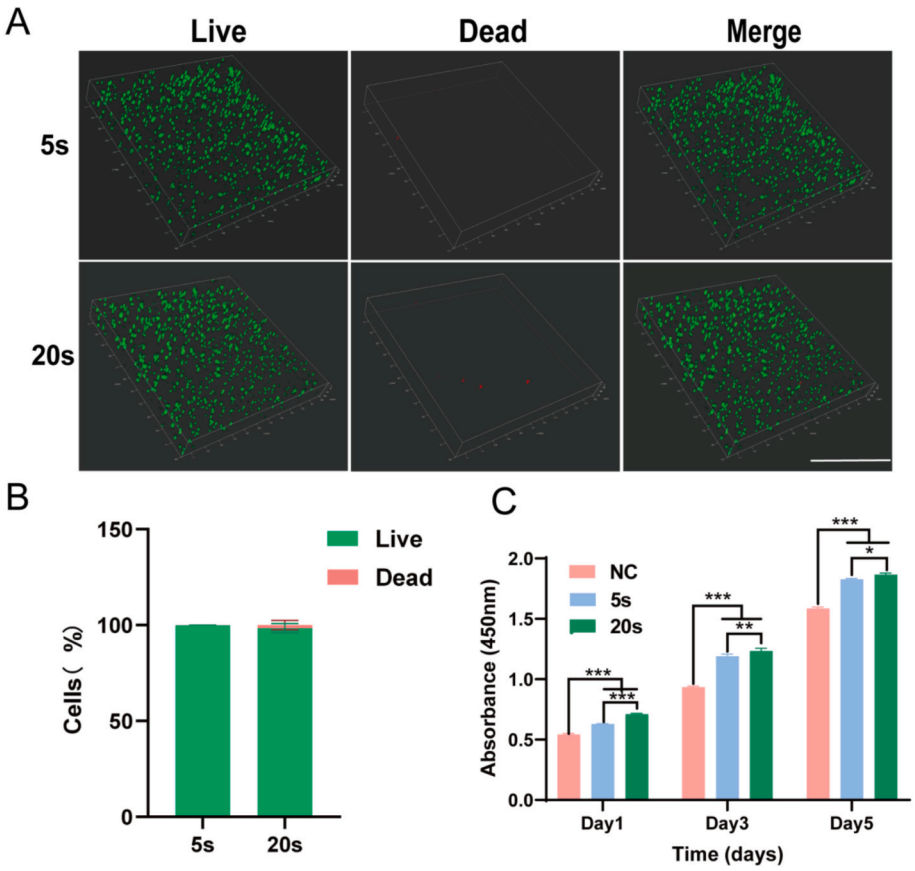

Fig. 3. Biocompatibility of BMSCs-loaded composite hydrogels with different modulus. A) and B) Live/Dead staining images and quantitative analysis of BMSCs cultured on composite hydrogels with different modulus for 5 days (scale bar: 500 μm). C) CCK-8 assay was performed at 1, 3, and 5 days of culture to measure cell viability in each group ($n = 3$). (*$p < 0.05$, **$p < 0.01$, ***$p < 0.001$).

the expression levels of *Col I*, *Runx2*, and *Ocn* were significantly higher in the 20s group than in both the 5 s and NC groups. In contrast, expression in the 5 s group showed a slight decrease compared to the NC group. Additionally, *Col X*, a marker gene for hypertrophic chondrocyte differentiation [56], was significantly upregulated in the 20s group, while the expression level in the 5 s group was similar to that of the NC group. Western Blot (Fig. 4E-H) results were consistent with the RT-qPCR findings. BMSCs cultured in 3D hydrogels (5 s and 20s) exhibited significantly enhanced chondrogenic differentiation compared to those cultured in 2D. The 5 s group showed upregulation of *Col II* and *Sox9* protein expression, along with suppression of *Col I* and *Col X*. In contrast, the 20s group not only upregulated *Col II* and *Sox9* protein expression but also promoted the expression of *Col I*, *Runx2*, *Ocn*, and *Col X* proteins. Furthermore, the results of immunofluorescence staining (Fig. 4I,J) and quantitative analysis (Fig. 4K,L) also demonstrated the expression of chondrocyte-related markers in different treatment groups (NC group, 5 s group, 20s group). The results showed that in the NC group, cells mainly expressed *Col I* and *Col X*, and almost no *Col II* was observed. In the 5 s group, the fluorescence signal of *Col II* was significantly enhanced. This suggests that the 5 s condition promoted chondrogenesis. In the 20s group, the fluorescence intensities of *Col I*, *Col II*, and *Col X* were all significantly increased. The quantitative analysis results were consistent with the fluorescence images. These results suggest that while the 20s hydrogel induces chondrogenic differentiation, it also significantly promotes osteogenic and hypertrophic chondrocyte differentiation, which may be detrimental to maintaining cartilage phenotype stability. The 5 s hydrogel, on the other hand, not only promotes BMSC chondrogenic differentiation but also effectively inhibits hypertrophic cartilage and osteogenic differentiation, making it more beneficial for growth plate cartilage repair.

3.6. Expression of the Piezo1-ROCK pathway in scaffold materials of each group

The Piezo1 ion channel and its downstream RhoA-ROCK signaling pathway play important roles in cellular mechanosensation [57,58]. Previous studies have shown that higher matrix stiffness can activate the Piezo1 channel, thereby stimulating the downstream RhoA-ROCK pathway and enhancing osteogenic differentiation [59,60]. As shown in Fig. 5A, RT-qPCR results revealed that the mRNA expression levels of Piezo1, RhoA, and ROCK1 were lower in the low-modulus 5 s hydrogel group than in both the control (NC) and high-modulus 20s groups. The mRNA expression level of Rac-1 was lower in the 5 s group than in the 20s group, and there was no significant difference compared to the NC group. In contrast, in the higher modulus 20s hydrogel group, the expression levels of Piezo1, RhoA, and Rac-1 were significantly upregulated, and all were higher than those in the NC and 5 s groups. Furthermore, Western Blot results (Fig. 5B-C) confirmed that protein levels of Piezo1, RhoA, and ROCK1 were significantly lower in the 5 s group compared to both NC and 20s, consistent with the RT-qPCR findings. These results suggest that the high-modulus hydrogel may enhance cellular mechanosignaling through the Piezo1-ROCK pathway, thereby promoting osteogenic differentiation. While the low-modulus hydrogel fails to significantly trigger this signaling pathway. This potentially favors cartilage phenotype stability [61,62] and thus promotes the repair of growth plate injuries.

3.7. In vivo cartilage regeneration ability of BMSCs-loaded scaffold materials in each group

A New Zealand white rabbit femoral defect model was established to

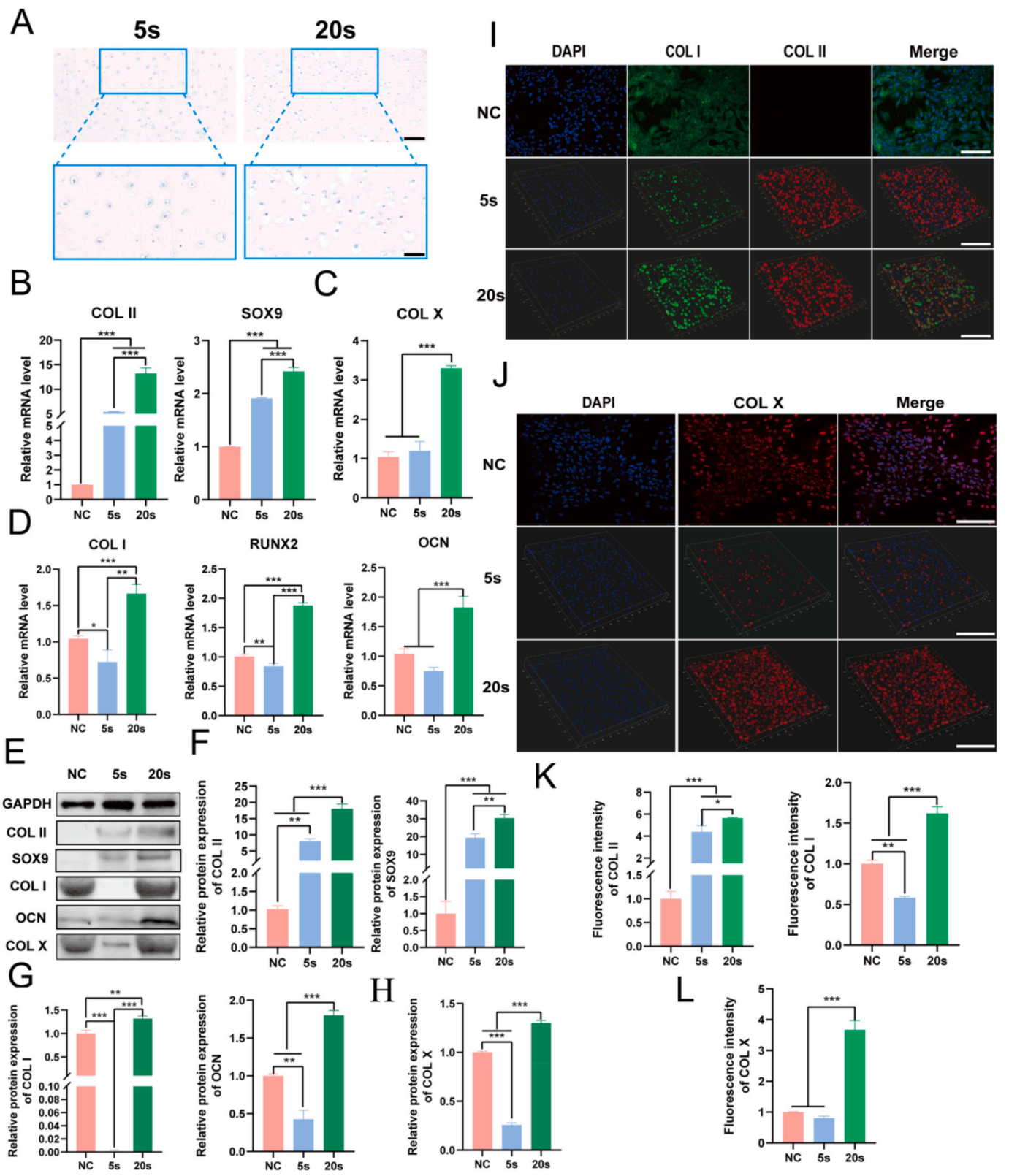

Fig. 4. Chondrogenic Differentiation of BMSCs on Different Modulus Composite Hydrogels *In Vitro*. A) Alcian Blue staining images of each group (original image scale bar: 100 μm; magnified image scale bar: 50 μm). B), C), and D) Expression levels of cartilage, hypertrophic cartilage, and osteogenesis-related genes after 14 days of culture ($n = 3$). E) Western Blot analysis of chondrogenic, osteogenic, and hypertrophic cartilage markers after 14 days of culture. F), G), and H) Quantification of chondrogenic, osteogenic, and hypertrophic cartilage-related protein expression ($n = 3$). I) Fluorescence images of chondrogenic and osteogenic markers (NC scale bar: 75 μm; 5 s and 20s scale bar: 200 μm). J) Fluorescence images of hypertrophic cartilage markers (NC scale bar: 75 μm; 5 s and 20s scale bar: 200 μm). K) and L) Quantification of the expression of chondrogenic, osteogenic, and hypertrophic cartilage markers by fluorescence ($n = 3$). (*$p < 0.05$, **$p < 0.01$, ***$p < 0.001$).

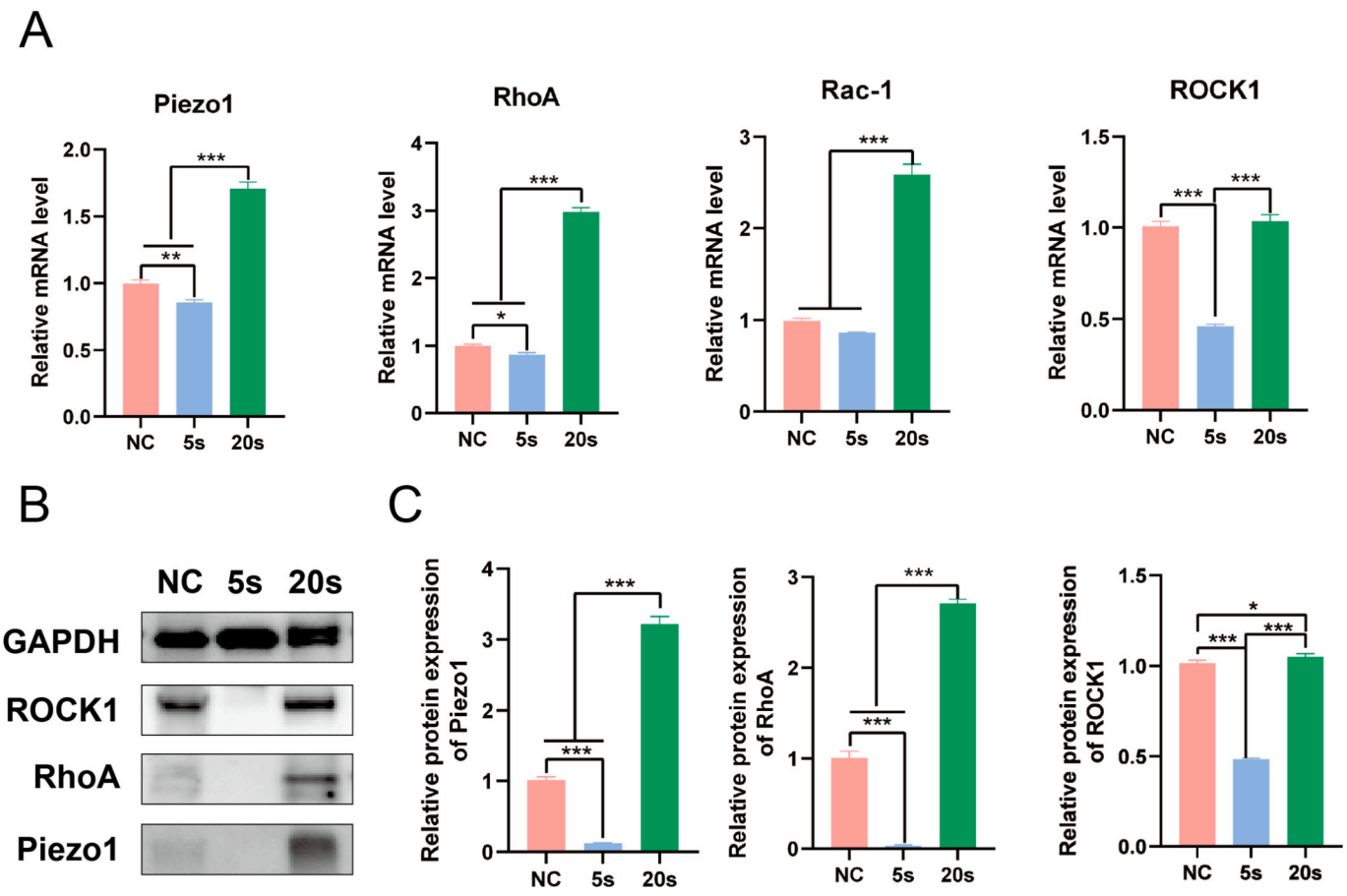

Fig. 5. Expression of the Piezo1-ROCK Pathway.A) Expression levels of pathway-related genes after 14 days of culture on composite hydrogels in each group ($n = 3$). B) and C) Western Blot analysis and quantitative results of pathway-related proteins after 14 days of culture ($n = 3$). (*$p < 0.05$, **$p < 0.01$, ***$p < 0.001$).

assess the ability of BMSCs-loaded composite hydrogels with different moduli to repair growth plate injuries. As shown in Fig. 6A, micro-CT images were used to evaluate bone bridging and cartilage regeneration in the defect area. The results showed that in the untreated control group (NC), the tibial growth plate defect area formed extensive bone formation, leading to severe collapse of the overall structure and angular deformities. In the higher modulus 20s group, both bone tissue and cartilage formation were observed in the defect area, and the degree of deformity was significantly reduced compared to the NC group. In contrast, the lower modulus 5 s group exhibited only cartilage formation without bone tissue occlusion, while the overall structure remained stable without collapse or deformity. Additionally, quantitative analysis by micro-CT also revealed significant differences among the groups. As shown in Fig. S5A, the bone volume fraction (BV/TV) in the NC group was markedly higher than in the 5 s and 20s groups, while the 20s group was significantly higher than the 5 s group. Similarly, bone mineral density (Tb.BMD, Fig. S5B) was highest in the NC group and lowest in the 5 s group. These results indicate that the low-modulus hydrogel (5 s) can effectively reduce bone bridge formation and is favorable for growth plate repair.

Histological sections and staining analyses were performed on tibial growth plate defect samples at 1 and 3 months post-surgery. H&E and Masson staining showed (Figs. 6B-C) that in the NC control group, the histological results at both 1 month and 3 months showed limited growth plate regeneration. The defect area showed almost no new cartilage cell formation and was filled with extensive bone formation. In the experimental groups, the low modulus 5 s hydrogel showed significant cartilage regeneration ability. Within 1 month post-surgery, this group exhibited a large number of newly formed cartilage cells in the defect area, and the cartilage tissue was evenly formed. By 3 months, the defect area was almost filled with cartilage-like tissue, with almost no abnormal bone growth observed. In contrast, although the high modulus 20s hydrogel showed some cartilage regeneration at both 1 and 3 months post-surgery, it was still accompanied by some bone tissue formation. Notably, at 3 months, the defect area in this group showed significant bone formation and mild collapse deformities. These results suggest that the mechanical modulus of the hydrogel plays an important role in growth plate injury repair, and an appropriate mechanical microenvironment is crucial for growth plate repair. The low modulus 5 s hydrogel was more effective in promoting cartilage tissue regeneration and reducing ectopic bone growth, showing better growth plate repair outcomes. However, the high modulus 20s hydrogel, although also having some repair ability, may lead to partial ossification due to the excessively rigid mechanical environment.

Toluidine Blue (TB) staining also confirmed the findings from H&E and Masson staining. The 20s group showed atypical cartilage regeneration. The 5 s group exhibited the least bone bridging and demonstrated the best growth plate cartilage repair (Figs. 6D). Furthermore, we quantitatively evaluated the defect area healing of different treatment groups at 1 and 3 months to assess the effectiveness of growth plate defect repair. As shown in Fig. S6A, at 1 month, the NC group exhibited a relatively large defect area (approximately 45 %). The 5 s group showed a significant reduction to less than 10 %, and the 20s group also decreased to about 15 %. At 3 months (Fig. S6B), the defect areas of all groups were further reduced. However, the 5 s group still demonstrated the best repair outcome (around 5 %), which was markedly better than the 20s group (approximately 12 %) and the NC group (about 30 %). Therefore, according to the statistical analysis revealed that the 5 s group was significantly superior to both the 20s and NC groups at both time points. This indicates that the low-modulus 5 s hydrogel has a

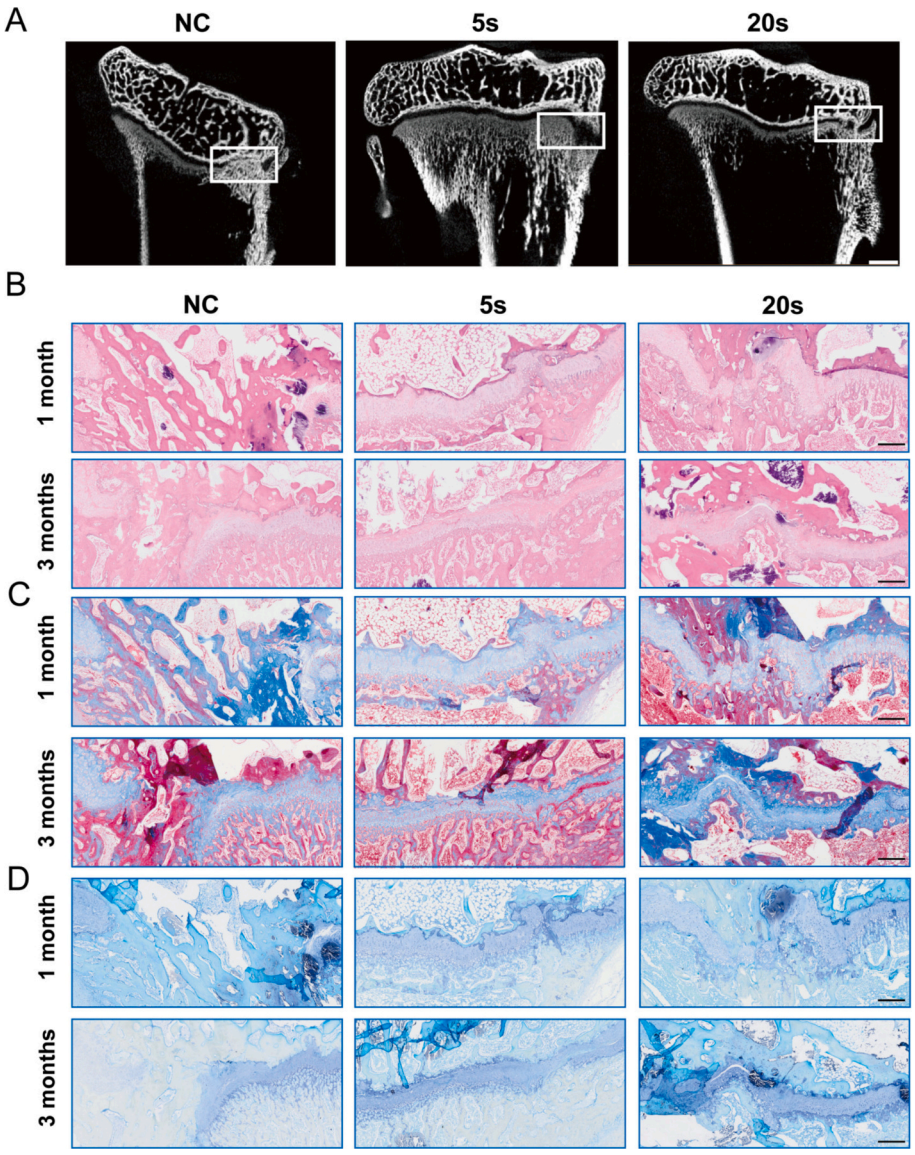

Fig. 6. Effects of BMSCs-loaded composite hydrogels with different moduli implanted into a growth plate defect model in New Zealand rabbits. A) Representative micro-CT images of each group (scale bar: 1 mm). B)、C) and D) Representative H&E、Masson and TB staining images of each group at 1 and 3 months post-implantation(scale bar: 300 μm).

greater advantage in promoting growth plate repair.

In summary, the low modulus 5 s hydrogel loaded with BMSCs effectively reduced bone bridging in New Zealand rabbits, promoted growth plate cartilage regeneration, and held promising clinical application potential.

4. Discussion

Growth plate injuries typically occur in children and adolescents, which can lead to bone bridge formation and limb growth deformities, seriously affecting the quality of life of patients [63]. Growth plate chondrocytes depend on a highly hydrated, three-dimensional extracellular matrix (ECM) microenvironment for survival. This unique physiological context poses significant functional reconstruction challenges. Consequently, traditional clinical and tissue engineering strategies struggle to achieve effective repair. Studies have shown that the ECM contains abundant active components—including collagen, proteoglycans, glycosaminoglycans, and growth factors. Beyond providing structural support, these components establish a biomimetic microenvironment that guides cell differentiation and improves cell survival [64]. Its successful application in muscle [65], bone [66], and articular cartilage [67] repair has confirmed the unique advantages of ECM as a scaffold for growth plate tissue engineering [30]. James et al. further pointed out that key components of ECM (such as collagen and glycosaminoglycans) are crucial for growth plate development [68]. Based on this, this study used porcine auricular cartilage to prepare ACM to overcome the limitations of autologous cartilage. This material significantly reduces immunogenicity by eliminating cellular components [16] while retaining key bioactive factors [17]. However, the poor mechanical stability of ACM hinders its application [18]. Therefore, we developed MA-modified ACMMA and combined it with GelMA to construct a three-dimensional biomimetic hydrogel scaffold, GelMA-ACMMA [69].

It is worth noting that the mechanical properties of three-dimensional hydrogels play a key regulatory role in the fate of stem cells. In this study, three-dimensional hydrogel scaffolds with different moduli were prepared by controlling the photopolymerization time. *In vitro* experiments showed that BMSCs cultured in 3D hydrogels had significantly enhanced proliferation and chondrogenic differentiation compared to those cultured in 2D. Additionally, the results indicated that the low modulus group (5 s) significantly upregulated the

expression of chondrogenic markers *(Sox9, Col II)* and inhibited osteogenic differentiation, while the high modulus group (20s) showed an osteogenic tendency. This phenomenon is consistent with previous studies: a low modulus environment (2 kPa) promotes chondrogenic differentiation, while a high modulus (60 kPa) induces osteogenesis [25]. To further verify the hydrogels' growth plate repair potential, we established a growth plate defect model in New Zealand rabbits. We subsequently conducted a systematic evaluation of the repair efficacy of hydrogels with varying moduli in an *in vivo* environment using micro-CT imaging and histological analysis. The results showed that the low modulus hydrogel could effectively promote cartilage regeneration in the defect area, significantly inhibit bone bridge formation, and maintain the integrity of the growth plate structure. However, the high modulus hydrogel, although it could induce the formation of cartilage tissue, was accompanied by bone bridge formation to a certain extent, leading to local collapse and deformity in the repair area. This result suggests that an appropriate mechanical microenvironment is crucial for growth plate repair, and a softer hydrogel is very suitable for maintaining the natural structure and function of the growth plate.

This study also further explored the role of the Piezo1-ROCK signaling pathway in the regulation of growth plate repair by hydrogels. The results showed that the Piezo1-ROCK pathway was not activated in the low modulus group, which helped maintain the stability of the chondrocyte phenotype. Conversely, in the higher modulus group, it might sense the viscoelastic changes of the matrix through Piezo1 and regulate intracellular Ca^{2+} signaling [26], thereby influencing the differentiation direction. This is consistent with the mechanical response characteristics of Piezo1 reported by Wu et al. [27], and explains the osteogenic tendency observed in the high modulus group: activation of Piezo1 can enhance osteogenic ability [28]. However, whether low modulus hydrogels have the ability to actively inhibit this pathway has not been fully verified. Future studies can clarify the specific regulatory mechanisms of different modulus hydrogels on the Piezo1-ROCK signaling axis through gene knockout or drug inhibition strategies. In addition, the bidirectional differentiation characteristics of chondrogenesis and osteogenesis exhibited by high modulus hydrogels during the growth plate repair process provide new research ideas for the repair of osteochondral tissues. In osteochondral tissue engineering, there are significant differences in the mechanical property requirements of different osteochondral interface tissue regions. How to achieve the coordinated regeneration of cartilage and bone tissues within the same material system is currently a major challenge. High modulus hydrogels, by mechanically regulating the directed differentiation of BMSCs, are expected to play a unique role in the repair of osteochondral interfaces, articular cartilage defects, and fractures. Future research can improve material design by combining gene or drug control strategies to develop composite scaffolds with gradient mechanical properties and biological activity, providing efficient and safe solutions for personalized osteochondral repair.

5. Conclusion

In summary, this study successfully developed composite hydrogels with varying stiffnesses loaded with BMSCs. *In vitro* experiments demonstrated that 3D hydrogels with varying stiffness exhibited good biocompatibility and the ability to promote BMSCs differentiation into chondrocytes. *In vivo* studies further confirmed their effectiveness in repairing growth plate injuries. Moreover, the study preliminarily revealed the potential mechanism by which the mechanical microenvironment of the hydrogels regulates BMSC fate through the Piezo1-ROCK signaling pathway. Future research will focus on the precise regulation of the Piezo1-ROCK pathway by hydrogels and explore their potential application in osteochondral repair and joint tissue engineering. This work provides both theoretical support and a material foundation for the clinical treatment of growth plate injuries and other cartilage-related disorders.

CRediT authorship contribution statement

Guanlu Shen: Writing – original draft, Methodology, Data curation, Conceptualization. **Xinxin Si:** Supervision, Formal analysis, Conceptualization. **Lei Qiang:** Writing – original draft, Methodology, Formal analysis, Conceptualization. **Yihao Liu:** Supervision, Methodology. **Zhiyang Yin:** Writing – original draft, Methodology, Formal analysis, Conceptualization. **Jing Shan:** Formal analysis, Data curation. **Pengfei Zheng:** Writing – review & editing, Supervision, Funding acquisition, Formal analysis, Conceptualization.

Declaration of competing interest

The authors declare that they have no known competing financial interests or personal relationships that could have appeared to influence the work reported in this paper.

Acknowledgements

This work was supported by the 16th special grant of China Postdoctoral Science Foundation (2023 T160331) and the 72nd General grant of China Postdoctoral Science Foundation (2022 M721685).

Appendix A. Supplementary data

Supplementary data to this article can be found online at https://doi.org/10.1016/j.cej.2025.168275.

Data availability

Data will be made available on request.

References

[1] L.P. Browne, R.P. Guillerman, R.C. Orth, et al., Community-acquired staphylococcal musculoskeletal infection in infants and young children: necessity of contrast-enhanced MRI for the diagnosis of growth cartilage involvement, Am. J. Roentgenol. 198 (1) (2012) 194–199.
[2] Y. Weitao, C. Qiqing, G. Songtao, et al., Epiphysis preserving operations for the treatment of lower limb malignant bone tumors, European Journal of Surgical Oncology (EJSO) 38 (12) (2012) 1165–1170.
[3] N. Shaw, C. Erickson, S.J. Bryant, et al., Regenerative medicine approaches for the treatment of pediatric physeal injuries, Tissue Eng. Part B Rev. 24 (2) (2017) 85–97.
[4] C.B. Erickson, J.P. Newsom, N.A. Fletcher, et al., In vivo degradation rate of alginate–chitosan hydrogels influences tissue repair following physeal injury, J Biomed Mater Res B Appl Biomater 108 (6) (2020) 2484–2494.
[5] C.B. Erickson, N. Shaw, N. Hadley-Miller, et al., A rat tibial growth plate injury model to characterize repair mechanisms and evaluate growth plate regeneration strategies, JoVE 125 (2017) e55571.
[6] P. Guan, Y. Ji, X. Kang, et al., Biodegradable dual-cross-linked hydrogels with stem cell differentiation regulatory properties promote growth plate injury repair via controllable three-dimensional mechanics and a cartilage-like extracellular matrix, ACS Appl. Mater. Interfaces 15 (7) (2023) 8986–8998.
[7] Z. Wang, Z. Li, Z. Li, et al., Cartilaginous extracellular matrix derived from decellularized chondrocyte sheets for the reconstruction of osteochondral defects in rabbits, Acta Biomater. 81 (2018) 129–145.
[8] A. Barmada, T. Gaynor, S.J. Mubarak, Premature Physeal closure following distal tibia Physeal fractures: a new radiographic predictor, J. Pediatr. Orthop. 23 (6) (2003).
[9] S. Muruganandan, R. Pierce, D.A. Teguh, et al., A FoxA2+ long-term stem cell population is necessary for growth plate cartilage regeneration after injury, Nat. Commun. 13 (1) (2022) 2515.
[10] P. Das, Y.P. Singh, B.B. Mandal, et al., Tissue-derived decellularized extracellular matrices toward cartilage repair and regeneration[M], Methods in cell biology: Academic Press 157 (2020) 185–221.
[11] X. Wang, Z. Li, C. Wang, et al., Enlightenment of growth plate regeneration based on cartilage repair theory: a review, Front. Bioeng. Biotechnol. 9 (2021) 654087.
[12] Y. Yu, K.M. Fischenich, S.A. Schoonraad, et al., A 3D printed mimetic composite for the treatment of growth plate injuries in a rabbit model, NPJ Regen. Med. 7 (1) (2022) 60.
[13] R. Ao, W. Liang, Z. Wang, et al., Delivery strategies of growth factors in cartilage tissue engineering, Tissue Eng. Part B, Rev. 16 (2024).
[14] L. Qiang, M. Fan, Y. Wang, et al., Injectable hydrogel loaded with bilayer microspheres to inhibit angiogenesis and promote cartilage regeneration for repairing growth plate injury, Front. Bioeng. Biotechnol. 11 (2023) 1181580.

[15] Z. Wang, J. Xu, J. Zhu, et al., Osteochondral tissue engineering: scaffold materials, fabrication techniques and applications, Biotechnol. J. 20 (1) (2025) e202400699.
[16] M. Kawecki, W. Łabuś, A. Klama-Baryla, et al., A review of decellurization methods caused by an urgent need for quality control of cell-free extracellular matrix' scaffolds and their role in regenerative medicine, J Biomed Mater Res B Appl Biomater 106 (2) (2018) 909–923.
[17] H. Hrebikova, D. Diaz, J. Mokry, Chemical decellularization: a promising approach for preparation of extracellular matrix, Biomedical papers 159 (1) (2015) 012–017.
[18] M. Brown, J. Li, C. Moraes, et al., Decellularized extracellular matrix: new promising and challenging biomaterials for regenerative medicine, Biomaterials 289 (2022) 121786.
[19] D.T. Chu, T.N.T. Phuong, N.L.B. Tien, et al., An update on the progress of isolation, culture, storage, and clinical application of human bone marrow mesenchymal stem/stromal cells, Int. J. Mol. Sci. 21 (3) (2020) 708.
[20] X. Chen, Y. Jiang, Y. Duan, et al., Mesenchymal-stem-cell-based strategies for retinal diseases, Genes 13 (10) (2022) 1901.
[21] H.J. Liao, C.H. Chang, C.Y.F. Huang, et al., Potential of using infrapatellar–fat–pad–derived mesenchymal stem cells for therapy in degenerative arthritis: chondrogenesis, exosomes, and transcription regulation, Biomolecules 12 (3) (2022) 386.
[22] S.S. Lee, G.E. Choi, H.J. Lee, et al., Layered double hydroxide and polypeptide Thermogel nanocomposite system for Chondrogenic differentiation of stem cells, ACS Appl. Mater. Interfaces 9 (49) (2017) 42668–42675.
[23] X. Li, Y. Xia, Z. Wang, et al., Three-dimensional matrix stiffness-based stem cell soil: tri-phase biomechanical structure promoted human dental pulp stem cells to achieve pulpodentin regeneration, Materials Today Bio 31 (2025) 101591.
[24] S.M. Naqvi, L.M. McNamara, Stem cell mechanobiology and the role of biomaterials in governing mechanotransduction and matrix production for tissue regeneration, Front. Bioeng. Biotechnol. 8 (2020) 597661.
[25] J.H. Galarraga, R.C. Locke, C.E. Witherel, et al., Fabrication of MSC-laden composites of hyaluronic acid hydrogels reinforced with MEW scaffolds for cartilage repair, Biofabrication 14 (1) (2022) 014106.
[26] R. Hao, H. Tang, C. Ding, et al., A novel Piezo1 agonist promoting mesenchymal stem cell proliferation and osteogenesis to attenuate disuse osteoporosis, Small Science 4 (9) (2024) 2400061.
[27] Z. Wu, Z. Yang, D. Sha, et al., Injectable, viscoelastic hydrogel precisely regulates developmental tissue regeneration, Chem. Eng. J. 434 (2022) 133860.
[28] B. Wang, G. Li, Q. Zhu, et al., Bone repairment via mechanosensation of Piezo1 using wearable pulsed triboelectric nanogenerator, Small 18 (30) (2022) 2201056.
[29] M. Kuwahara, Y. Akasaki, N. Goto, et al., Fluvastatin promotes chondrogenic differentiation of adipose-derived mesenchymal stem cells by inducing bone morphogenetic protein 2, BMC Pharmacol. Toxicol. 23 (1) (2022) 61.
[30] L. Jia, Y. Hua, J. Zeng, et al., Bioprinting and regeneration of auricular cartilage using a bioactive bioink based on microporous photocrosslinkable acellular cartilage matrix, Bioactive Materials 16 (2022) 66–81.
[31] X. Yu, X. Wang, D. Li, et al., Mechanically reinforced injectable bioactive nanocomposite hydrogels for in-situ bone regeneration, Chem. Eng. J. 433 (2022) 132799.
[32] L. Fan, C. Liu, X. Chen, et al., Directing induced pluripotent stem cell derived neural stem cell fate with a three-dimensional biomimetic hydrogel for spinal cord injury repair, ACS Appl. Mater. Interfaces 10 (21) (2018) 17742–17755.
[33] P. Guan, C. Liu, D. Xie, et al., Exosome-loaded extracellular matrix-mimic hydrogel with anti-inflammatory property facilitates/promotes growth plate injury repair, Bioactive Materials 10 (2022) 145–158.
[34] R.M. Coleman, J.E. Phillips, A. Lin, et al., Characterization of a small animal growth plate injury model using microcomputed tomography, Bone 46 (6) (2010) 1555–1563.
[35] N.K. Singh, W. Han, S.A. Nam, et al., Three-dimensional cell-printing of advanced renal tubular tissue analogue, Biomaterials 232 (2020) 119734.
[36] N. Bhamare, K. Tardalkar, P. Parulekar, et al., 3D printing of human ear pinna using cartilage specific ink, Biomed. Mater. 16 (5) (2021) 055008.
[37] H. Kim, B. Kang, X. Cui, et al., Light-activated decellularized extracellular matrix-based bioinks for volumetric tissue analogs at the centimeter scale, Adv. Funct. Mater. 31 (32) (2021) 2011252.
[38] G. Zu, M. Meijer, O. Mergel, et al., 3D-printable hierarchical nanogel-GelMA composite hydrogel system, Polymers 13 (15) (2021) 2508.
[39] E. Yuce-Erarslan, T. Rumeysa, İ. Burçin, et al., Photo-crosslinkable chitosan and gelatin-based nanohybrid bioinks for extrusion-based 3d-bioprinting, Int. J. Polym. Mater. Polym. Biomater. 72 (1) (2023) 1–12.
[40] X. Si, Q. Zhang, B. Ning, et al., Injectable photocrosslinkable acellular cartilage matrix hydrogel loaded with exosomes for promoting growth plate injury repair, Chem. Eng. J. 493 (2024) 152463.
[41] Y. Zhang, H. Leng, Z. Du, et al., Efficient regeneration of rat calvarial defect with gelatin-hydroxyapatite composite cryogel, Biomed. Mater. 15 (6) (2020) 065005.
[42] F.C. Dos Santos, S.V. Harb, M.J. Menu, et al., On the structure of high performance anticorrosive PMMA–siloxane–silica hybrid coatings, RSC Adv. 5 (129) (2015) 106754–106763.
[43] D. Hamulić, P. Rodič, M. Poberžnik, et al., The effect of the methyl and ethyl group of the acrylate precursor in hybrid silane coatings used for corrosion protection of aluminium alloy 7075-T6, Coatings 10 (2) (2020) 172.
[44] J. Huo, H. Zeng, A novel triphenylamine functionalized bithiazole–metal complex with C 60 for photocatalytic hydrogen production under visible light irradiation, J Mater Chem A 3 (12) (2015) 6258–6264.
[45] N. Huebsch, P.R. Arany, A.S. Mao, et al., Harnessing traction-mediated manipulation of the cell/matrix interface to control stem-cell fate, Nat. Mater. 9 (6) (2010) 518–526.
[46] E. Omidvari, M. Samandari, D. Ghanbariamin, et al., Nanoliposome functionalized colloidal GelMA inks for 3D printing of scaffolds with multiscale porosity, Biofabrication 17 (1) (2025) 015039.
[47] B. Li, H. Qin, M. Ma, et al., Preparation of novel β-CD/P(AA-co-AM) hydrogels by frontal polymerization, RSC Adv. 13 (9) (2023) 5667–5673.
[48] D. Choi, J. Heo, J. Aviles Milan, et al., Structured nanofilms comprising Laponite® and bone extracellular matrix for osteogenic differentiation of skeletal progenitor cells, Mater. Sci. Eng. C 118 (2021) 111440.
[49] X. Liu, T. Li, H. Guo, et al., Co3o4/carbon nanohybrids embedded in the fibrous scaffolds promote stem cell osteogenic differentiation via strengthening cell mechanotransduction, Colloid Interface Sci Commun, Colloid Interface Sci Commun 52 (2023) 100682.
[50] M. Ghanbari, M. Salavati-Niasari, F. Mohandes, et al., Modified silicon carbide NPs reinforced nanocomposite hydrogels based on alginate-gelatin by with high mechanical properties for tissue engineering, Arab. J. Chem. 15 (1) (2022) 103520.
[51] A. Berradi, F. Aziz, M.E. Achaby, et al., A comprehensive review of polysaccharide-based hydrogels as promising biomaterials, Polymers 15 (13) (2023) 2908.
[52] Y. Zhang, K. Kobayashi, M. Wada, Comparative analysis of the structures and properties of cellulose hydrogels prepared using different solvent systems, Cellulose 32 (4) (2025) 2337–2351.
[53] R. Chung, C.J. Xian, RECENT RESEARCH ON THE GROWTH PLATE: mechanisms for growth plate injury repair and potential cell-based therapies for regeneration, J. Mol. Endocrinol. 53 (1) (2014) T45–T61.
[54] J.B. Studdert, H. Bildsoe, V.P. Masamsetti, et al., Craniofacial Development: Methods and Protocols, in: Visualization of the Cartilage and Bone Elements in the Craniofacial Structures by Alcian Blue and Alizarin Red Staining, 2022, pp. 43–50.
[55] F.H. Zhou, B.K. Foster, G. Sander, et al., Expression of proinflammatory cytokines and growth factors at the injured growth plate cartilage in young rats, Bone 35 (6) (2004) 1307–1315.
[56] S. van Eegher, M.L. Perez-Lozano, I. Toillon, et al., The differentiation of prehypertrophic into hypertrophic chondrocytes drives an OA-remodeling program and IL-34 expression, Osteoarthr. Cartil, Osteoarthr. Cartil. 29 (2) (2021) 257–268.
[57] B. Xie, X. He, Y. Guo, et al., Cyclic tensile stress promotes osteogenic differentiation via upregulation of Piezo1 in human dental follicle stem cells, Hum. Cell 37 (6) (2024) 1649–1662.
[58] Q. Gao, M. Wang, X. Hou, et al., Substrate stiffness modulates osteogenic and adipogenic differentiation of osteosarcoma through PIEZO1 mediated signaling pathway, Cell. Signal. 127 (2025) 111601.
[59] Y. Zou, X. Zeng, K. Wang, et al., CD271 regulates osteogenic differentiation of ectomesenchymal stem cells via the RhoA/ROCK signaling pathway, Int. Immunopharmacol. 148 (2025) 114068.
[60] Q. Lu, J. Diao, Y. Wang, et al., 3D printed pore morphology mediates bone marrow stem cell behaviors via RhoA/ROCK2 signaling pathway for accelerating bone regeneration, Bioactive Materials 26 (2023) 413–424.
[61] T. Zhang, T. Gong, J. Xie, et al., Softening substrates promote chondrocytes phenotype via RhoA/ROCK pathway, ACS Appl. Mater. Interfaces 8 (35) (2016) 22884–22891.
[62] J. Yang, L. Wang, Z. Zhang, et al., Downregulation of HAS-2 regulates the chondrocyte cytoskeleton and induces cartilage degeneration by activating the RhoA/ROCK signaling pathway, Int. J. Mol. Med. 52 (1) (2023) 57.
[63] Y.H. Guo, Y.B. Yu, J.J. Wu, et al., Curdlan/chitosan NIR-responsive in situ forming gel: an injectable scaffold for the treatment of epiphyseal plate injury, Int. J. Biol. Macromol. 308 (2025) 142052.
[64] F. Mercier, Fractones: extracellular matrix niche controlling stem cell fate and growth factor activity in the brain in health and disease, Cell. Mol. Life Sci. 73 (24) (2016) 4661–4674.
[65] Y.-J. Choi, Y.-J. Jun, D.Y. Kim, et al., A 3D cell printed muscle construct with tissue-derived bioink for the treatment of volumetric muscle loss, Biomaterials 206 (2019) 160–169.
[66] G.M. Cunniffe, P.J. Díaz-Payno, E.J. Sheehy, et al., Tissue-specific extracellular matrix scaffolds for the regeneration of spatially complex musculoskeletal tissues, Biomaterials 188 (2019) 63–73.
[67] L. Peng, H. Li, H. Deng, et al., Combination of a human articular cartilage-derived extracellular matrix scaffold and microfracture techniques for cartilage regeneration: a proof of concept in a sheep model, Journal of Orthopaedic Translation 44 (2024) 72–87.
[68] J. Melrose, C. Shu, J.M. Whitelock, et al., The cartilage extracellular matrix as a transient developmental scaffold for growth plate maturation, Matrix Biol. (2016) 363–383, 52-54.
[69] Z. Dong, Q. Yuan, K. Huang, et al., Gelatin methacryloyl (GelMA)-based biomaterials for bone regeneration, RSC Adv. 9 (31) (2019) 17737–17744.